Theoretical prediction of two-dimensional $1T$-MSiN$_3$ (M = V, Nb) with direct bandgap and long carrier lifetime

Luo Yan [1,2] Anqi Huang,[1,2] Bao-Tian Wang [3] Jian-Guo Si [3] Yi-min Ding [1,*] and Liujiang Zhou [1,2,†]

[1]*Yangtze Delta Region Institute (Huzhou), University of Electronic Science and Technology of China, Huzhou 313001, China*
[2]*School of Physics, University of Electronic Science and Technology of China, Chengdu 611731, China*
[3]*Institute of High Energy Physics, Chinese Academy of Science (CAS), Beijing 100049, China*

Motivated by the discoveries on the two-dimensional (2D) MoSi$_2$N$_4$ family [Y. L. Hong *et al.*, Science **369**, 670 (2020)] that can be regarded as 2D transition-metal dinitrides (MN$_2$) attached by Si-N layers on its two sides, in this work, we propose an emerging 2D MSiN$_3$ family, where only one side of MN$_2$ monolayer passivated via a Si-N layer. Among them, $1T$-VSiN$_3$ and $1T$-NbSiN$_3$ monolayer are determined to be direct-gap semiconductors with a bandgap of 1.24 and 2.92 eV, respectively, calculated on the Heyd-Scuseria-Ernzerhof hybrid functional level. In addition, $1T$-VSiN$_3$ and $1T$-NbSiN$_3$ monolayer are nonmagnetic within its ground state, and can maintain the chemical, dynamical, thermal, as well as mechanical stability. In the framework of quantum many-body perturbation theory, $1T$-VSiN$_3$ and $1T$-NbSiN$_3$ monolayer display strong light-harvesting ability in visible-light region, and have a long carrier lifetime up to the nanosecond level, suggestive of a high light-to-current conversion efficiency. This finding broadens the 2D semiconductors with excellent optical features, and would trigger more interest in this emerging family of MSiN$_3$ materials.

I. INTRODUCTION

The layered transition-metal dinitrides (MN$_2$) with a rhombohedral MoS$_2$ crystal, namely, $3R$-MoN$_2$, have been synthesized via a solid-state ion exchange reaction [1]. Thus, the MN$_2$ in an atomic scale as shown Fig. 1(a) could be produced by exfoliating from layered phase [2,3], similar to the common synthesis routes for MoS$_2$ monolayer (ML) or multilayers [4–6]. As a consequence, the research on two-dimensional (2D) MN$_2$ sprang up like mushrooms. For instance, ferromagnetic (FM) $2H$-MoN$_2$ ML has a very high Curie temperature (420 K) [2]. The simultaneous isostructural and magnetic phase transition can be realized in MoN$_2$ ML with a moderate strain [7]. Single-layer (SL) $1T$-TaN$_2$ is a FM half-metal with a bandgap of 0.72 eV, along with a high Curie temperature (339 K) [8]. In addition, $1T$-LaN$_2$ ML is a Dirac spin-gapless semiconductor and Chern insulator with a high Chern number [9]. SL metallic $2H$- and $1T$-TaN$_2$ MLs turn to superconducting states at low temperatures [10]. All in all, by the choice of transition-metal component, MN$_2$ MLs exhibit rich electronic properties, including metal, half-metal, semiconducting, and superconducting states [7,8,10–12]. However, MN$_2$ MLs usually lack a reliable chemical stability, due to the unsaturated $2p$ orbitals of surface-terminated N atoms. But, as a two-edged sword, the dangling orbitals in two-dimensional (2D) MN$_2$ offer a chance to design novel 2D materials via adopting surface modifications or adsorptions.

Recently, MoSi$_2$N$_4$ ML has been effectively obtained in the centimeter scale, via a novel chemical vapor deposition growth method [13]. This exotic structure can be regarded as a MoN$_2$ ML saturated by the Si-N layers on its two sides, forming a seven-atom-layered 2D material [Fig. 1(c)]. Compared with the freestanding MN$_2$ ML, the Si-N layers bring a great chemical stability with saturated surfaces in the MoSi$_2$N$_4$ family, as well as significantly improved mechanical and thermal stability. On the other hand, MN$_2$ MLs passivated by Si-N layers also yield fascinating physiochemical features, such as valley polarization [14–16], highly efficient photocatalysts [17,18], topological states [19], intrinsic piezoelectricity [20], selective adsorption of molecules [21], nonlinear optical response [22], high and anomalous thermal conductivity [23], as well as greatly enhanced superconductivity [10,19], etc. However, the lack of direct-gap semiconductors among the MSi$_2$N$_4$ family limits their applications in photoelectric field [13]. As we know, 2D Ga$_2$N$_3$ has been realized via graphene encapsulation, which can be viewed as a Ga-N layer attached on only one side of GaN$_2$ ML [24]. More recently, Si-N layers bring superconductivity, semiconducting states, and ternary valley structure in graphene, via passivating its two sides step by step [25]. Naturally a question arises: Can other 2D MN$_2$ MLs be passivated by only one Si-N layer, thus leading to an emerging 2D MSiN$_3$ family of materials, analogous to the crystals of 2D Ga$_2$N$_3$?

In this work, we systematically study the structural and electronic properties of a 2D MSiN$_3$ family of materials, where M represents the early transition metals with the advantages of being rich and eco-friendly. This family of materials has only one Si-N layer attached on the surface of 2D MN$_2$. After high-throughput calculations, we find that SL $1T$-VSiN$_3$
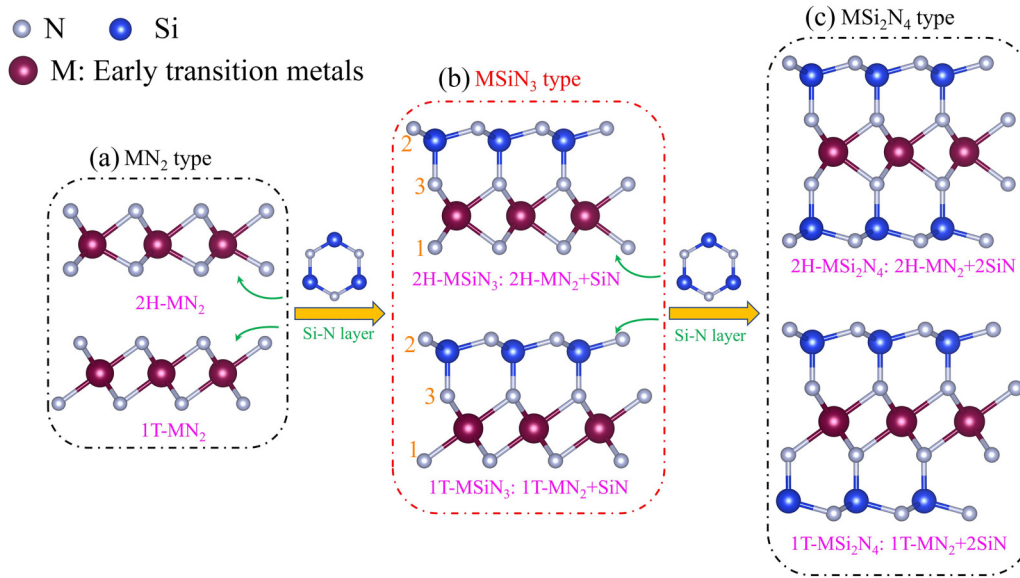
* ymding00@qq.com
† liujiang86@gmail.com

FIG. 1. The crystals of $M\mathrm{SiN}_3$ MLs from side view are displayed in (b). $M\mathrm{N}_2$ and $M\mathrm{Si}_2\mathrm{N}_4$ MLs are also presented in (a) and (c), respectively. The 2H and 1T phases are depicted in the upper and lower panel, respectively.

and $1T$-NbSiN_3 have high stability and direct bandgaps of 1.24 and 2.92 eV, respectively, at the Heyd-Scuseria-Ernzerhof hybrid functional (HSE06) level. Moreover, they display excellent visible-light absorption ability upon including electron-hole (e-h) interactions. In addition, via the nonadiabatic molecular dynamics (NAMD) simulations, their carrier lifetimes show significant variations at the nanosecond level. The underlying nonradiative coupling (NAC) and pure-dephasing times are clearly compared to elucidate their e-h recombinations.

II. COMPUTATIONAL METHODS

The first-principles calculations were performed by means of density functional theory, utilizing the Vienna *ab initio* simulation package (VASP) [26,27]. The ion-electron interactions were treated with the projector augmented-wave pseudopotentials [27,28]. The exchange-correlation potentials were considered on the basis of generalized gradient approximation, formalized by Perdew-Burke-Ernzerhof (PBE) [29]. The plane-wave energy cutoff and Γ-centered k-point grid were set to be 500 eV and $25\times25\times1$, respectively. The optB88-vdw method and dipole moment corrections were considered in all calculations. In addition, the structural model was separated by 15 Å vacuum space along the z direction. In order to modify the bandgap values, the HSE06 method was further considered [30]. The *ab initio* molecular dynamics (AIMD) simulations were performed to study the thermal properties, and a $4\times4\times1$ supercell was adopted. In the framework of density functional perturbation theory, the features of phonons were carried out with the PHONOPY code [31]. Moreover, the HIPHIVE package was used to deal with the high-temperature phonon calculations [32]. As implemented in YAMBO software [33], the $\mathrm{G}_0\mathrm{W}_0$ approximation within many-body perturbation theory along with the random phase approximation (RPA) or Bethe-Salpeter equation (BSE) was used to study the optical properties without or with e-h interactions. Furthermore, the

NAMD was performed via HEFEI-NAMD code to simulate the carrier lifetime [34]. More detailed computational methods are provided in the Supplemental Material [35].

III. RESULTS AND DISCUSSION

A. Dynamical stability and electronic features of SL MiSiN$_3$ family

The artificial SL $M\mathrm{SiN}_3$ models are depicted in Fig. 1(b), where M represents the early transition metals, such as Sc, Y, Ti, Zr, Hf, V, Nb, Ta, Cr, Mo, and W. In the framework of a typically structural foundation of $M\mathrm{N}_2$ type [Fig. 1(a)], $M\mathrm{SiN}_3$ MLs also can possess two general phases: 2H trigonal prismatic and 1T octahedral phases [Fig. 1(b)]. These two phases crystallize in a hexagonal lattice and share the same space group of $P3m1$ (No. 156) with a C_{3v} point symmetry. They are constructed by attaching a Si-N layer on only one surface of $M\mathrm{N}_2$ MLs. A similar rule is adopted for synthesizing $\mathrm{MoSi}_2\mathrm{N}_4$ MLs, which can be viewed as a MoN_2 passivated by Si-N layers on its two sides [13]. There are three types of N atoms, assigned a label N^i with $i = 1$–3, in which the N^1 atoms bond with the M atoms, and the N^2 and Si atoms fall into the Si-N layer; N^3 connects the upper hexagonal Si-N_2 layer and M atoms.

In order to clearly capture the basic characteristics among the SL $M\mathrm{SiN}_3$ family, we systematically study their dynamical stability and electronic structures. Based on the optimized SL $M\mathrm{SiN}_3$ crystals, phonon spectra are firstly performed to verify their kinetic stability. All dynamically stable phases are listed in Supplemental Material Table S1, verfied by the phonon spectra (see Supplemental Material Figs. S1–S4) [35]. Among them, SL 1T-$M\mathrm{SiN}_3$ with M atoms in groups IVB and VB are determined to be dynamically stable, while 2H-$M\mathrm{SiN}_3$ MLs with M atoms only in the group VB are dynamically stable. But, 1T- and 2H-$M\mathrm{SiN}_3$ MLs in groups IIIB and VIB and 2H phases in group IVB are unstable. In our high-throughput calculations, nonmagnetic (NM) and

TABLE I. Symmetry, vibration, activity, and frequency (THz) for the 12 optical vibrational modes at the Γ point in SL $1T$-VSiN$_3$.

Modes	Symmetry	Vibration	Activity	Frequency
(4, 5)	E	In-plane V, Si, N^2	IR	3.98
(6)	A_1	Out-of-plane V, Si, N^2	IR	10.08
(7, 8)	E	In-plane N^3	IR	10.39
(9, 10)	E	In-plane N^1	IR	15.51
(11)	A_1	Out-of-plane N^1	IR	19.18
(12)	A_1	Out-of-plane Si, N^2	IR	20.32
(13, 14)	E	In-plane Si, N^2	IR	24.96
(15)	A_1	Out-of-plane N^3	IR	29.36

FM spin configurations were considered. SL $1T$-MSiN$_3$ (M = Ti, Zr, Hf) is FM, whereas $1T$- and $2H$-MSiN$_3$ (M = V, Nb, Ta) MLs have NM ground state. The magnetic moments in FM MLs mostly originate from the N^1-$2p$ orbitals. On the other hand, due to the weaker electronegativity of M in group VB and the decrease of charge transfer between M and N^1 atoms, SL MSiN$_3$ (M = V, Nb, Ta) have NM ground states. Further electron property investigations reflect FM $1T$-MSiN$_3$ (M = Ti, Zr, Hf) MLs behave metallic features with a mount of spin-up electronic states crossing the Fermi level (see Supplemental Material Fig. S2) [35]. In contrast, SL $1T$- and $2H$-MSiN$_3$ (M = V, Nb, Ta) are semiconductors (see Supplemental Material Fig. S3) [35], whose bandgaps are in the range of 1.24–3.38 eV at the HSE06 level (Table I). The diverse electronic properties of SL MSiN$_3$ arise from the progressive filling of the M-d bands from groups IIIB to VB. When the orbitals are partially filled, $1T$-MSiN$_3$ (M = Ti, Zr, Hf) MLs exhibit metallic properties. When the orbitals are fully occupied, MSiN$_3$ (M = V, Nb, Ta) MLs are semiconductors. In particular, SL $1T$-VSiN$_3$ and $1T$-NbSiN$_3$ are direct semiconductors with a bandgap of 1.24 and 2.92 eV (HSE06), respectively, favoring their underlying performance in the next-generation optoelectronic nanodevices.

B. Atomic structures for SL $1T$-VSiN$_3$ and $1T$-NbSiN$_3$

Given that SL $1T$-VSiN$_3$ and $1T$-NbSiN$_3$ have great potential in the optoelectronic field, we mainly focus on them in the following. The lattice of SL $1T$-VSiN$_3$ is optimized to be $a = b = 2.90$ Å, which is relatively smaller than that of SL $1T$-NbSiN$_3$ (3.04 Å), due to the larger atomic radii of Nb atoms. As the electron localization function (ELF) [36] plots in Supplemental Material Fig. S5 [35] show, the Si-N^2 and Si-N^3 bonds exhibit a strong covalent trait, verified by the strongly localized electron distribution residing at the center area of bonds. The Si-N^2 and Si-N^3 distances of 1.75/1.82 Å and 1.74/1.75 Å in $1T$-VSiN$_3$/NbSiN$_3$ ML also confirm the covalent feature. The M-N^1 and M-N^3 (M = V, Nb) bonds possess the ionic feature due to the preference of electron distribution toward N and M atoms, respectively. This is also supported by the M-N^1 and M-N^3 distances, of about 1.98 and 2.09 Å in SL $1T$-VSiN$_3$ and $1T$-NbSiN$_3$, respectively. Moreover, N^1-N^3 and M-M distances are larger than 2.81 Å, showing no significant interactions. In terms of Bader charge calculations [37] for SL $1T$-VSiN$_3$/$1T$-NbSiN$_3$, V/Nb atom

donates 1.06/1.3e to the N^1 atom and 0.81/1.00e to the N^3 atom; the Si atom transfers 0.76/0.74e to the N^3 atom and 2.22/2.17e to the N^2 atom. Clearly, the amount of transferred charges in $1T$-VSiN$_3$ ML (4.85e) is smaller than that in SL $1T$-NbSiN$_3$ (5.21e).

C. The stability from chemical, dynamical, thermal, and mechanical aspects

Since the stability is a fundamental factor for materials in practical applications, we have systemically explored the chemical, dynamical, thermal, and mechanical stabilities of SL $1T$-VSiN$_3$ and $1T$-NbSiN$_3$. Firstly, to study the chemical stability of SL $1T$-VSiN$_3$ and NbSiN$_3$, the adsorption energies (E_{ad}) of four general functional groups (FGs) (i.e., -F, -H, -O, and -OH groups) adsorbed on the unpassivated N^1 atoms are evaluated via

$$E_{ad} = E_{\text{system}} - E_{M\text{SiN}_3} - E_{FG}, \quad (1)$$

where E_{system} and $E_{M\text{SiN}_3}$ respectively denotes the energy of adsorbed and unadsorbed $1T$-MSiN$_3$ within a $3 \times 3 \times 1$ supercell. The energies of E_{FG} are derived from the chemical potential of F$_2$, H$_2$, and O$_2$, and then the energy of the OH group can be calculated as $E_{\text{OH}} = E_{\text{H}_2\text{O}} - E_{\text{H}}$. The calculated E_{ad} of the -F, -H, -O, and -OH groups for SL $1T$-VSiN$_3$/NbSiN$_3$ are -0.11/0.42, -0.06/-0.01, -0.26/0.20, and 1.42/2.15 eV, respectively. Therefore, $1T$-VSiN$_3$ and $1T$-NbSiN$_3$ MLs are more inclined to maintain their free-standing phase, rather than be functionalized by the functional groups.

No imaginary frequencies confirm the dynamical stability for SL $1T$-VSiN$_3$ [Fig. 2(a)] and $1T$-NbSiN$_3$ [Fig. 2(b)]. Since a primitive cell has five atoms, there are 15 phonon modes: 3 acoustic and 12 optical branches. Three acoustic branches mostly contributed by V/Nb atoms are constituted by the out-of-plane, in-plane transverse, and in-plane longitudinal modes. Due to the existence of C_{3v} point-group symmetry in $1T$-MSiN$_3$ MLs, four nondegenerate and four doubly degenerate optical phonon modes at the Γ point can be decomposed as

$$\Gamma_{\text{optical}} = 4A_1(IR) + 4E(IR), \quad (2)$$

where I and R represent infrared and Raman-active modes, respectively. Obviously, these 12 optical branches of SL $1T$-VSiN$_3$ at the Γ point obtain infrared and Raman-active modes simultaneously. To directly reflect the relative motions of V, Si, and N atoms, their vibration modes at the Γ point are visualized in Figs. 2(c)–2(j). For instance, the doubly degenerate (4, 5) modes at 3.98 THz are dominated from the in-plane vibrations of V, Si, and N^2 atoms. For 11th modes at 19.18 THz, the vibration modes are mostly from N^1 atoms, along the out-of-plane direction. More information about their vibration features at the Γ point are given in Table I, where symmetry, vibration, Raman, and infrared activity are listed. Due to same crystal symmetry in $1T$-MSiN$_3$ ML, the vibrational properties of SL $1T$-NbSiN$_3$ can be inferred from $1T$-VSiN$_3$ ML reasonably.

The energies of $1T$-VSiN$_3$ and $1T$-NbSiN$_3$ MLs slightly fluctuate around the equilibrium energy value during the entire simulation period and there are no signs of structural
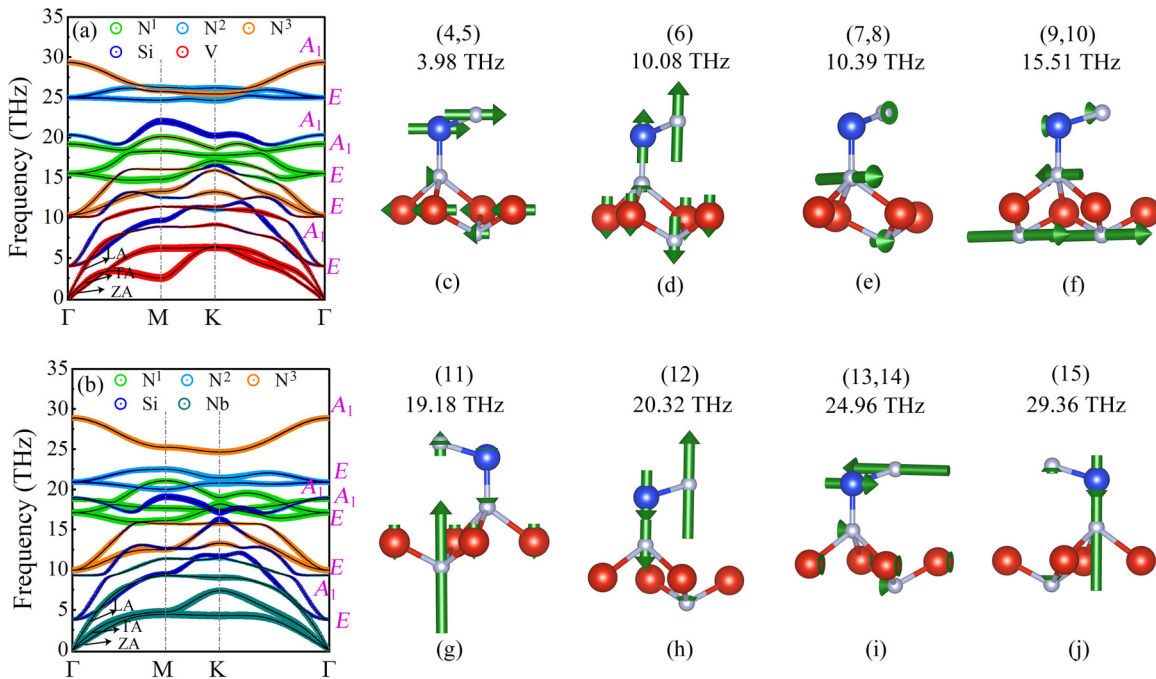
FIG. 2. The projected phonon spectra of (a) $1T$-VSiN$_3$ and (b) $1T$-NbSiN$_3$, weighted by their constituted atoms. (c)–(j) The vibration modes at the Γ point for optical branches.

disruptions after annealing at 2100 K [Figs. 3(a) and 3(d)]. However, at 2400 K, the M-N^1 bonds are distorted to a large extent. Therefore, they can maintain structural integrity at

an extremely high melting point (2100–2400 K), favoring further fabrications and applications at high temperatures. In this regard, the Si-N layer attached on the surface of the
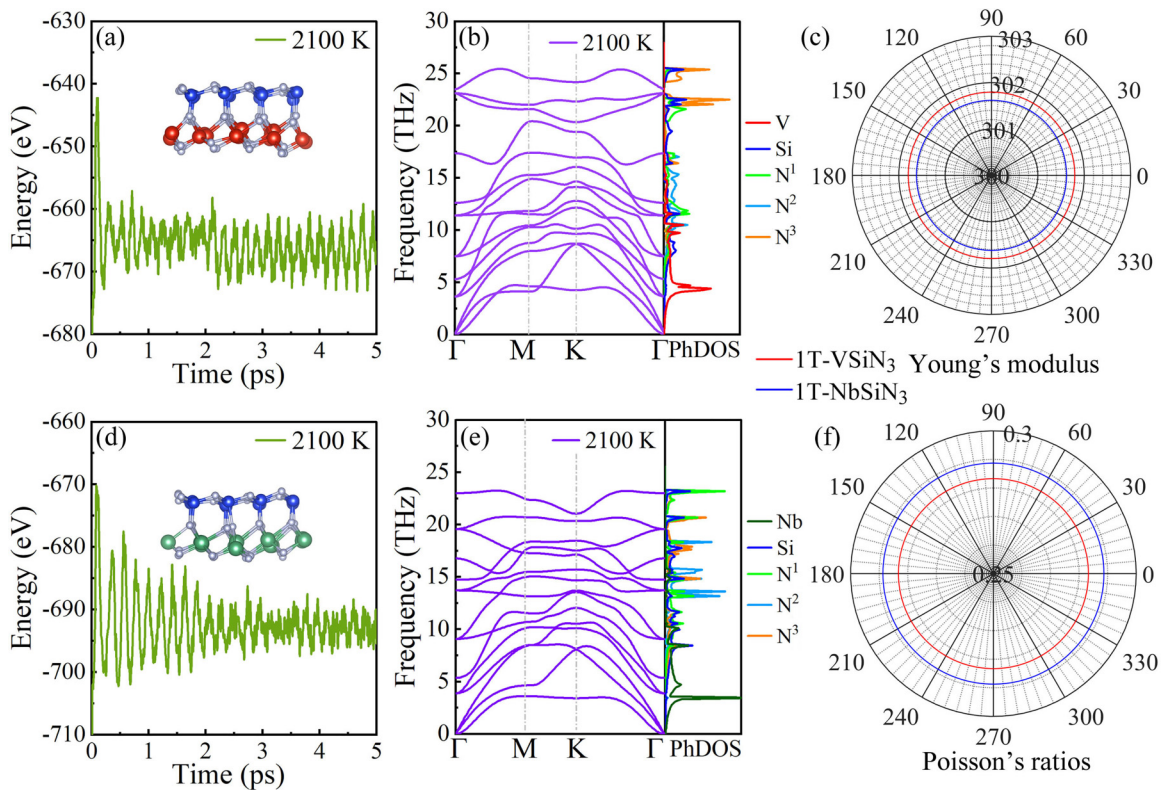

FIG. 3. The variations of energy for (a) $1T$-VSiN$_3$ and (d) $1T$-NbSiN$_3$ MLs during the AIMD simulation, along with the last snapshots from the side view. The calculated phonon spectra at 2100 K and the corresponding PhDOS for (b) $1T$-VSiN$_3$ and (e) $1T$-NbSiN$_3$ MLs. The orientation-dependent Young's modulus and Poisson's ratios are plotted in (c) and (f), respectively.
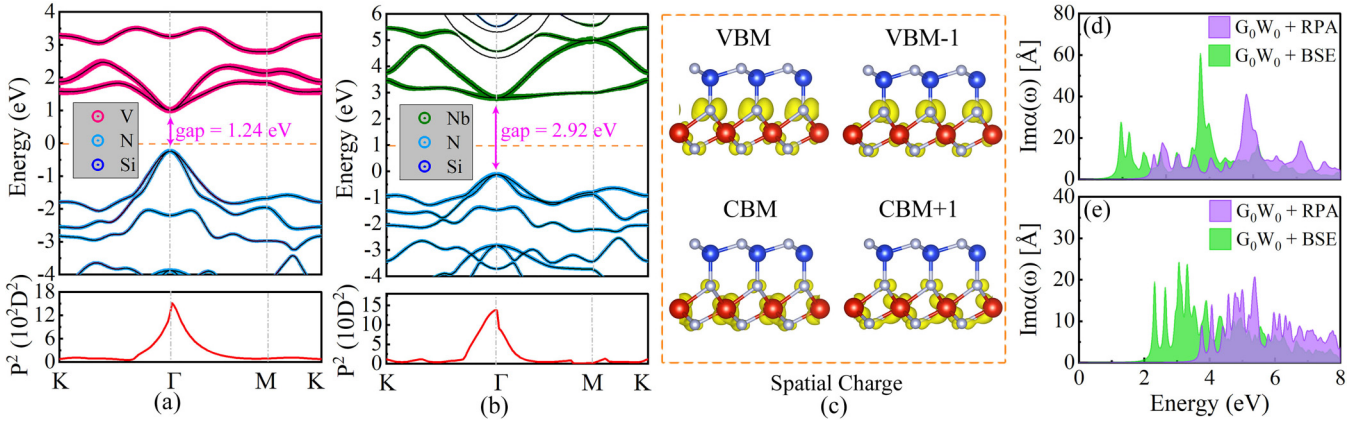
FIG. 4. The projected band structures magnitude by their component atoms (upper plane) and calculated dipole transition dipole moment P^2 (lower plane) at the HSE06 level for (a) $1T$-$VSiN_3$ and (b) $1T$-$NbSiN_3$. Spatial charge distributions of doubly degenerate VBM and CBM states for (a) $1T$-$VSiN_3$. The imaginary part of the macroscopic polarizability for (d) $1T$-$VSiN_3$ and (e) $1T$-$NbSiN_3$, simulated at G_0W_0+RPA and G_0W_0+BSE levels.

$1T$-NbN_2 ML strongly improves the thermal stability, as SL $1T$-NbN_2 is not stable at room temperature [8]. In addition, the phonon spectra calculated at 2100 K also support their outstanding stability [Figs. 3(b) and 3(e)]. Compared with the phonon spectra at 0 K, the optical branches shift down about 4 THz towards the lower frequency region, reflecting weaker bonding interactions at high temperature. This is due to the thermal effects leading to more active atomic vibrations and larger atomic distances between component atoms. As indicated in the projected phonon density of states (PhDOS) at 2100 K, the contribution of each type of atom locates at their relative position, relying on their atomic mass.

As listed in Table S2, $1T$-$VSiN_3$ and $1T$-$NbSiN_3$ MLs satisfy the Born criteria, $C_{11}^2 > C_{12}^2$ and $C_{66} > 0$ [38], suggesting they maintain mechanical stability. Based on the calculated C_{ij} values, the orientation-dependent Young's modulus $Y(\theta)$ and Poisson's ratios $\nu(\theta)$ as a function of the polar angle can be expressed as

$$Y(\theta) = \frac{C_{11}^2 - C_{12}^2}{C_{11}\sin^4(\theta) + A_1\cos^2(\theta)\sin^2(\theta) + C_{11}\cos^4(\theta)} \quad (3)$$

and

$$\nu(\theta) = \frac{C_{12}\cos^4(\theta) - A_2\cos^2(\theta)\sin^2(\theta) + C_{11} + C_{12}\sin^4(\theta)}{C_{11}\sin^4(\theta) + A_1\cos^2(\theta)\sin^2(\theta) + C_{11}\cos^4(\theta)}, \quad (4)$$

respectively, where A_1 and A_2 are defined as $A_1 = (C_{11}^2 - C_{12}^2)/C_{66} - 2 \times C_{12}$ and $A_2 = 2 \times C_{11} - (C_{11}^2 - C_{12}^2)/C_{66}$, respectively. As clearly shown in Figs. 3(c) and 3(f), both Y and ν show isotropic characters with perfect circles in the polar diagram. Moreover, the mechanical properties of $1T$-$VSiN_3$ and $1T$-$NbSiN_3$ MLs are almost identical, with only a 0.92 N/m difference in Y and a 0.01 difference in ν. The obtained Y values for SL $1T$-$VSiN_3$ and $1T$-$NbSiN_3$ are about 302 N/m, larger than that of $1T$-TaN_2 (162 N/m), but smaller than SL $1T$-$TaSi_2N_4$ (455 N/m) and $1T$-$NbSi_2N_4$ (449 N/m) MLs [10]. Thus, the Si-N layers lead to a higher stiffness.

D. Electronic and optical properties

Now, we turn to their electronic properties. SL $1T$-$VSiN_3$ and $1T$-$NbSiN_3$ are direct bandgap semiconductors with valence band maximum (VBM) and conduction band minimum (CBM) locating at the Γ point [Figs. 4(a) and 4(b)]. The calculations of the transition dipole moment (P^2) also mean directly allowed electronic transition between VBM and CBM at the Γ point. The doubly degenerate VBM and CBM are preserved by crystal symmetry, and respectively dominated by the orbitals of N and V atoms, indicating the efficient separation of electron and hole carriers. Moreover, the real-space partial charge density plots of $1T$-$VSiN_3$ in Fig. 4(c) show that the VBM and VBM -1 states are composed of $p_{x,y}$ orbitals of N^3 atoms mostly and N^1 atoms partially. For the CBM and CBM $+1$ states, the V-$d_{xz,yz}$ orbitals play a major role, and the $p_{x,y}$ orbitals of N^3 and N^1 atoms have little participation. In addition, the spatial charge distributions of SL $1T$-$NbSiN_3$ are similar to $1T$-$VSiN_3$ ML (see Supplemental Material Fig. S6) [35]. More importantly, SL $1T$-$VSiN_3$ has a direct bandgap of 1.24 eV, comparable to that of silicon in experiment (1.23 eV) [39]; $1T$-$VSiN_3$ ML possesses a direct bandgap of 2.92 eV, slightly larger than that of hittorfene (SL violet phosphorus; 2.71 eV) [40], MoS_2 (2.25 eV), and WS_2 (2.32 eV) [41] MLs at the HSE06 level. In addition, the effective masses for SL $1T$-$VSiN_3$ are $0.71m_0$ ($0.81m_0$) and $0.38m_0$ ($0.41m_0$) for electrons and holes along the x (y) direction [see Supplemental Material Fig. S7(a)] [35], which are smaller than that of hittorfene (0.69–$1.24m_0$) [40], and comparable to MX_2 ($M =$ Mo, W; $X=$ S, Se, Te) (0.24–$0.52m_0$) [42], SL black phosphorus (BP) (0.17–$1.12m_0$) [43], Tl_2O (0.10–$4.01m_0$) [44], and Sc_2CCl_2 (0.23–$2.26m_0$) [45] MLs. Interestingly, the effective masses for electrons and holes are highly isotropic [see Supplemental Material Fig. S7(d)] [35], coinciding with the nearly symmetric energy band structure around CBM and VBM [Fig. S7(b)]. However, as for $1T$-$NbSiN_3$ ML, the effective masses of electrons are $2.61m_0$ and $4.69m_0$ in the x and y directions, respectively, showing an anisotropic feature [see Supplemental Material Fig. S7(e)] [35]. On the other hand, the effective masses, both in electrons and holes, are

TABLE II. The energy of bandgap E_g at PBE and HSE06 levels (eV), the optical bandgap E_g^o (eV), G_0W_0 gap (eV), and the exciton binding energy E_b (eV) for $1T$-MSiN$_3$ (M = V, Nb) MLs.

Compounds	E_g (PBE)	E_g (HSE06)	E_g^o	G_0W_0 gap	E_b
$1T$-VSiN$_3$	0.66	1.24	0.97	1.58	0.61
$1T$-NbSiN$_3$	1.99	2.92	2.31	3.64	1.33

TABLE III. Averaged gaps in the whole AIMD process, absolute NA coupling (NAC), pure-dephasing time (T), and carrier lifetime (τ) for $1T$-VSiN$_3$ and $1T$-NbSiN$_3$ MLs at 300 K.

Compounds	Averaged gaps (eV)	NAC (meV)	T (fs)	τ (ns)
$1T$-VSiN$_3$	1.37	5.16	12.36	0.49
$1T$-NbSiN$_3$	3.34	1.39	19.21	60.16

slightly larger than those in $1T$-VSiN$_3$ ML, reflected by the flat band dispersion, especially for CBM [see Supplemental Material Fig. S7(c)] [35]. Given the suitable bandgaps and small effective masses, $1T$-VSiN$_3$ and $1T$-NbSiN$_3$ MLs have great potential in the optoelectronic field.

To consider the e-h interactions and reduced charge screening effects in our titled 2D systems, the G_0W_0 calculations are further adopted here. The imaginary parts of the macroscopic polarizability for $1T$-VSiN$_3$ and $1T$-NbSiN$_3$ MLs, which directly implies the light absorbance ability, are shown in Figs. 4(d) and 4(e), respectively. Some related parameters are given in Table II. SL $1T$-VSiN$_3$($1T$-NbSiN$_3$) has a quasiparticle energy gap (G_0W_0 gap) of 1.58 (3.64 eV), according to the spectral edge from G_0W_0 + RPA calculations. Obviously, the G_0W_0 approximation corrects the HSE06 bandgap value about 0.34 (0.72) eV. Based on the G_0W_0 and BSE calculations, the optical bandgap E_g^0, defined from the first absorption peak, is determined to be 0.97 and 2.31 eV for $1T$-VSiN$_3$ and $1T$-NbSiN$_3$ MLs, respectively. The lowest optically allowed peak for SL $1T$-VSiN$_3$ indicates it can absorb light in the infrared region originally. As for $1T$-NbSiN$_3$ ML, it has a larger E_g^0 and starts to absorb light in the visible-light region. In addition, the exciton binding energy (E_b) of SL $1T$-VSiN$_3$ is evaluated to be about 0.61 eV, comparable to that in 2D $1T$-Ti$_2$OF$_2$ (0.61 eV) [46], TiNCl (0.74 eV), TiNBr (0.66 eV) [47], MoS$_2$ (0.80 eV) [48], and Janus-MoSSe (0.95 eV) [49]. Due to the larger bandgap with weaker screening in $1T$-NbSiN$_3$ ML, its E_b is increased to be 1.33 eV. Clearly, SL $1T$-VSiN$_3$ and $1T$-NbSiN$_3$ have strong light absorbance ability in the visible-light region, and thus they can be used as solar energy materials. In addition, $1T$-VSiN$_3$ and $1T$-NbSiN$_3$ MLs are also promising for infrared and ultraviolet detectors, respectively, due to the excellent light absorption ability in the desired spectral range.

E. Carrier lifetimes simulations

As discussed above, $1T$-VSiN$_3$ and $1T$-NbSiN$_3$ MLs with strong visible-light absorption abilities, can be applied as solar energy materials. In this regard, the lifetime of the excited carrier is the most critical factor in light-to-current conversion efficiency. Meanwhile, the carrier lifetime is dominated by the radiative and nonradiative (NA) e-h recombination process. However, radiative e-h recombination is usually at the femtosecond scale, thus, the NA charge recombination is the dominating factor. The NA e-h recombination rate is strongly associated with the nonradiative coupling (NAC), which is defined as [34]

$$d_{ij} = \langle \varphi_j | \frac{\partial}{\partial t} | \varphi_k \rangle = \sum_I \frac{\langle \varphi_j | \nabla_{R_I} \mathcal{H} | \varphi_k \rangle}{\varepsilon_k - \varepsilon_j} \dot{\mathbf{R}}_I, \quad (5)$$

where $\mathcal{H}$ represents the Kohn-Sham Hamiltonian, and $\varphi_{j/k}$ and $\varepsilon_{j/k}$ are the wave functions and eigenvalues for electronic states j/k, respectively. Here, the states j and k indicate CBM and VBM, respectively. Therefore, the magnitude of the NAC is determined by the electron-phonon (e-ph) coupling elements ($\langle \varphi_j | \nabla_{R_I} \mathcal{H} | \varphi_k \rangle$), energy gap ($\varepsilon_k - \varepsilon_j$), and the nuclear velocity $\mathbf{R}_I$. As summarized in Table III, the NAC for SL $1T$-VSiN$_3$ (5.16 meV) is about four times larger than that in SL $1T$-NbSiN$_3$ (1.39 meV), hinting that the carrier lifetime should be longer in $1T$-NbSiN$_3$ ML [50].

Clearly, the NAC is proportional to the nuclear velocity $\dot{\mathbf{R}}_I$ and the time-dependent e-ph coupling elements $\langle \varphi_j | \nabla_{R_I} \mathcal{H} | \varphi_k \rangle$. Here, the $\dot{\mathbf{R}}_I$ is roughly proportional to $\sqrt{m}$, where m is the atomic mass [51], and thus the heavier Nb atom would slightly suppress the NAC in $1T$-NbSiN$_3$ ML. In addition, e-ph coupling elements determined by the e-ph interaction and the wave function overlap between VBM and CBM are further compared. As reported previously, the orbital distributions for VBM and CBM in $1T$-VSiN$_3$ and $1T$-NbSiN$_3$ MLs are similar [Figs. 4(c) and S6], and thus the wave function overlap plays a negligible role in this giant NAC difference. In particular, as shown in Figs. 5(a) and 5(b), the relatively larger amplitudes of the bandgap fluctuations in SL $1T$-NbSiN$_3$ characterize the stronger strength of the e-ph interaction. To reveal the dominating phonon modes that contribute to the e-ph coupling, the Fourier transform of its normalized autocorrelation functions (ACFs) are plotted in Fig. 5(c). For $1T$-VSiN$_3$ ML, a dominant phonon peak appears at around 4.8 THz, where the in-plane V, Si, and N^2 atom vibrations are engaged in the NA process mostly [Fig. 2(c)], while for SL $1T$-NbSiN$_3$, there is no dominant phonon peak in low frequency, due to the heavier atomic mass of Nb, prohibiting the activation of vibrations. But, the atom vibrations below the 10 THz frequency region contribute major rules in e-ph interaction. In this regard, the low-frequency vibrations in SL $1T$-VSiN$_3$/NbSiN$_3$ greatly stimulate the collisions between free carriers and phonons. But, higher frequency modes have little influence on NAC. More importantly, NAC is inversely proportional to the energy difference between CBM and VBM. The averaged bandgap for SL $1T$-NbSiN$_3$ is 1.37 eV, corrected by the G_0W_0, which is about three times smaller than SL $1T$-NbSiN$_3$ (3.34 eV). As a result, $1T$-VSiN$_3$ ML has a large NAC naturally.

Beyond the NACs, the pure-dephasing functions reflect loss of quantum coherence in the electronic subsystem due to coupling to phonons. And the pure-dephasing (also named as decoherence) times are much shorter than the e-h recombination times. Therefore, the carrier lifetimes are evaluated with inclusion of decoherence into the NAMD algorithm, as implemented in the HEFEI-NAMD code [34]. In the framework of
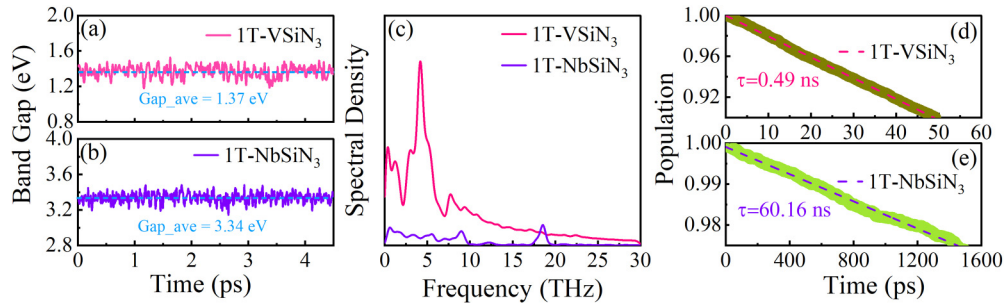
FIG. 5. The variations of bandgaps during the molecular dynamics for (a) $1T$-VSiN$_3$ and (b) $1T$-NbSiN$_3$ MLs, as well as the averaged bandgap values. (c) The spectral densities for the bandgaps. Time evolution of the hot electron population due to nonradiative e-h recombination in (d) $1T$-VSiN$_3$ and (e) $1T$-NbSiN$_3$ MLs.

the second-order cumulant approximation of optical response theory [52], the decoherence time was obtained by fitting the dephasing functions with a Gaussian, $\exp[-0.5(t/T)^2]$. As plotted in Supplemental Material Fig. S8(a) [35], the decoherence time for SL $1T$-VSiN$_3$ (12.36 fs) is slightly faster than that for SL $1T$-NbSiN$_3$ (19.21 fs). The fast dephasing time is associated with the large fluctuations between VBM and CBM [Figs. 5(a) and (5b)], and also supports the stronger e-ph interactions. In addition, the unnormalized ACFs (u-ACFs) decay on similar timescales [see Supplemental Material Fig. S8(b)] [35], while their initial values have an evident difference. Generally, a larger squared initial value of u-ACF that corresponds to the standard deviations of phonon-induced fluctuations of bandgaps, means a faster accumulation of the wave function phase difference, thus reflecting a shorter decoherence time [53,54]. Therefore, the initial value of u-ACF in SL $1T$-NbSiN$_3$ indicates a fast pure-dephasing process and a large gap fluctuation, coinciding with former results.

The evolutions of the excited electron state population are exhibited in Figs. 5(d) and 5(e). Here, the doubly degenerate VBM and CBM at 0 K are inclined to be nondegenerate as temperature is heated to 300 K, and thus have small influence on the carrier recombination rate [46]. Thus, one hot electron is presumed to relax from the nondegenerate VBM to the CBM state. By fitting a linear expansion of exponential decay, $f(t) = \exp(-t/\tau) \approx 1 - t/\tau$, the carrier lifetimes for $1T$-VSiN$_3$ and $1T$-NbSiN$_3$ MLs are evaluated to be 0.49 and 60.16 ns, respectively. Within the Marcus theory [55] and Fermi's golden rule [56], a weaker NAC and a faster pure-dephasing process would lead to a prolonged e-h recombination process. Here, more specifically, the smaller e-ph interactions in the low-frequency and larger bandgap regulate the weaker NAC in SL $1T$-NbSiN$_3$. However, a slightly lighter V atomic mass and faster quantum decoherence process in $1T$-VSiN$_3$ ML cannot delay carrier recombination significantly. Therefore, their instrinsic bandgaps are the primary factors for such a huge difference in carrier lifetimes. Numerically, their carrier lifetimes

reach the nanosecond scale, particularly for SL $1T$-NbSiN$_3$ (60.16 ns), which is much longer than that for pristine and doped BP (0.39–5.34 ns) [51], MoS$_2$ (0.39 ns) [57], Janus-MoSTe (1.31 ns) [48], Ti$_2$OF$_2$ (0.39–2.8 ns) ML [46], and even longer than that of MAPbI$_3$ perovskite (12.0 ns) [54], and BaZrS$_3$-based perovskites (6.83–33.88 ns) [58], favoring their exotic performances in optoelectronic fields.

IV. CONCLUSION

In conclusion, we have obtained two direct-gap semiconductors, $1T$-VSiN$_3$ and $1T$-NbSiN$_3$ MLs, by high-throughput calculations in the 2D $2H/1T$-MSiN$_3$ (M = early transition metal) family. SL $1T$-VSiN$_3$ and $1T$-NbSiN$_3$ are NM in their ground states, and behave with reliable stability from chemical, dynamical, mechanical, and thermal aspects. Within HSE06 level, the bandgap values for SL $1T$-VSiN$_3$ and $1T$-NbSiN$_3$ are 1.24 and 2.92 eV, respectively. Moreover, $1T$-VSiN$_3$ and $1T$-NbSiN$_3$ MLs possess pronounced visible-light absorption ability, implying their excellent application as light-harvesting candidates in solar field. The carrier lifetime of SL $1T$-NbSiN$_3$ (60.16 ns) is much longer than that for SL $1T$-VSiN$_3$ (0.49 ns), due to its intrinsic larger bandgap. Our work would provide promising candidates in optoelectronic nanodevices among the MSiN$_3$ family, and will stimulate more efforts on this emerging material.

[1] S. Wang, H. Ge, S. Sun, J. Zhang, F. Liu, X. Wen, X. Yu, L. Wang, Y. Zhang, H. Xu *et al.*, J. Am. Chem. Soc. **137**, 4815 (2015).

[2] F. Wu, C. Huang, H. Wu, C. Lee, K. Deng, E. Kan, and P. Jena, Nano Lett. **15**, 8277 (2015).

[3] M. Onodera, F. Kawamura, N. T. Cuong, K. Watanabe, R. Moriya, S. Masubuchi, T. Taniguchi, S. Okada, and T. Machida, APL Mater. **7**, 101103 (2019).

[4] J. N. Coleman, M. Lotya, A. O'Neill, S. D. Bergin, P. J. King, U. Khan, K. Young, A. Gaucher, S. De, R. J. Smith *et al.*, Science **331**, 568 (2011).

[5] G. Eda, H. Yamaguchi, D. Voiry, T. Fujita, M. Chen, and M. Chhowalla, Nano Lett. **11**, 5111 (2011).

[6] S. Ghatak, A. N. Pal, and A. Ghosh, ACS Nano **5**, 7707 (2011).

[7] Y. Wang, S.-S. Wang, Y. Lu, J. Jiang, and S. A. Yang, Nano Lett. **16**, 4576 (2016).

[8] J. Liu, Z. Liu, T. Song, and X. Cui, J. Mater. Chem. C **5**, 727 (2017).

[9] L. Li, X. Kong, X. Chen, J. Li, B. Sanyal, and F. M. Peeters, Appl. Phys. Lett. **117**, 143101 (2020).

[10] L. Yan, B.-T. Wang, X. Huang, Q. Li, K. Xue, J. Zhang, W. Ren, and L. Zhou, Nanoscale **13**, 18947 (2021).

[11] Y. Wang and Y. Ding, J. Phys. Chem. C **122**, 26748 (2018).

[12] Y. Sun, B. Xu, and L. Yi, Chin. Phys. B **29**, 023102 (2020).

[13] Y.-L. Hong, Z. Liu, L. Wang, T. Zhou, W. Ma, C. Xu, S. Feng, L. Chen, M.-L. Chen, D.-M. Sun *et al.*, Science **369**, 670 (2020).

[14] S. Li, W. Wu, X. Feng, S. Guan, W. Feng, Y. Yao, and S. A. Yang, Phys. Rev. B **102**, 235435 (2020).

[15] Q. Cui, Y. Zhu, J. Liang, P. Cui, and H. Yang, Phys. Rev. B **103**, 085421 (2021).

[16] J. Yuan, Q. Wei, M. Sun, X. Yan, Y. Cai, L. Shen, and U. Schwingenschlögl, Phys. Rev. B **105**, 195151 (2022).

[17] Y. Yu, J. Zhou, Z. Guo, and Z. Sun, ACS Appl. Mater. Interfaces **13**, 28090 (2021).

[18] C. Xiao, R. Sa, Z. Cui, S. Gao, W. Du, X. Sun, X. Zhang, Q. Li, and Z. Ma, Appl. Surf. Sci. **563**, 150388 (2021).

[19] L. Wang, Y. Shi, M. Liu, A. Zhang, Y.-L. Hong, R. Li, Q. Gao, M. Chen, W. Ren, H.-M. Cheng *et al.*, Nat. Commun. **12**, 2361 (2021).

[20] B. Mortazavi, F. Shojaei, B. Javvaji, T. Rabczuk, and X. Zhuang, Mater. Today Energy **22**, 100839 (2021).

[21] A. Bafekry, M. Faraji, M. Fadlallah, A. A. Ziabari, A. B. Khatibani, S. Feghhi, M. Ghergherehchi, and D. Gogova, Appl. Surf. Sci. **564**, 150326 (2021).

[22] J.-S. Yang, L. Zhao, L. Shi-Qi, H. Liu, L. Wang, M. Chen, J. Gao, and J. Zhao, Nanoscale **13**, 5479 (2021).

[23] Y. Yin, M. Yi, and W. Guo, ACS Appl. Mater. Interfaces **13**, 45907 (2021).

[24] Z. Y. Al Balushi, K. Wang, R. K. Ghosh, R. A. Vilá, S. M. Eichfeld, J. D. Caldwell, X. Qin, Y.-C. Lin, P. A. DeSario, G. Stone *et al.*, Nat. Mater. **15**, 1166 (2016).

[25] L. Yan, J. Zhu, B.-T. Wang, P.-F. Liu, G. Wang, S. A. Yang, and L. Zhou, Phys. Rev. B **107**, 085413 (2023).

[26] G. Kresse and J. Furthmüller, Phys. Rev. B **54**, 11169 (1996).

[27] G. Kresse and D. Joubert, Phys. Rev. B **59**, 1758 (1999).

[28] P. E. Blöchl, Phys. Rev. B **50**, 17953 (1994).

[29] J. P. Perdew, K. Burke, and M. Ernzerhof, Phys. Rev. Lett. **77**, 3865 (1996).

[30] A. V. Krukau, O. A. Vydrov, A. F. Izmaylov, and G. E. Scuseria, J. Chem. Phys. **125**, 224106 (2006).

[31] A. Togo and I. Tanaka, Scr. Mater. **108**, 1 (2015).

[32] F. Eriksson, E. Fransson, and P. Erhart, Adv. Theory Simul. **2**, 1800184 (2019).

[33] A. Marini, C. Hogan, M. Grüning, and D. Varsano, Comput. Phys. Commun. **180**, 1392 (2009).

[34] Q. Zheng, W. Chu, C. Zhao, L. Zhang, H. Guo, Y. Wang, X. Jiang, and J. Zhao, Wiley Interdiscip. Rev.: Comput. Mol. Sci. **9**, e1411 (2019).

[35] See Supplemental Material at http://link.aps.org/supplemental/10.1103/PhysRevB.108.155309 for computational methods via YAMBO and NAMD software, phonon spectra and band structures for SL MSiN$_3$ monolayers, ELF plots, spatial charge distributions, orientation-dependent effective mass for 1T-VSiN$_3$ and 1T-NbSiN$_3$ monolayers, pure-dephasing functions and unnormalized autocorrelation functions, optimized lattice constants, and elastic constants.

[36] A. Savin, R. Nesper, S. Wengert, and T. F. Fässler, Angew. Chem. Int. Ed. Engl. **36**, 1808 (1997).

[37] W. Tang, E. Sanville, and G. Henkelman, J. Phys.: Condens. Matter **21**, 084204 (2009).

[38] F. Mouhat and F.-X. Coudert, Phys. Rev. B **90**, 224104 (2014).

[39] J. W. Precker and M. A. da Silva, Am. J. Phys. **70**, 1150 (2002).

[40] G. Schusteritsch, M. Uhrin, and C. J. Pickard, Nano Lett. **16**, 2975 (2016).

[41] Y. Ding, Y. Wang, J. Ni, L. Shi, S. Shi, and W. Tang, Phys. B: Condens. Matter **406**, 2254 (2011).

[42] W. Zhang, Z. Huang, W. Zhang, and Y. Li, Nano Res. **7**, 1731 (2014).

[43] J. Qiao, X. Kong, Z.-X. Hu, F. Yang, and W. Ji, Nat. Commun. **5**, 4475 (2014).

[44] Y. Ma, A. Kuc, and T. Heine, J. Am. Chem. Soc. **139**, 11694 (2017).

[45] L. Zhou, Y. Zhang, Z. Zhuo, A. J. Neukirch, and S. Tretiak, J. Phys. Chem. Lett. **9**, 6915 (2018).

[46] L. Yan, J. Zhu, B.-T. Wang, J. He, H.-Z. Song, W. Chu, S. Tretiak, and L. Zhou, Nano Lett. **22**, 5592 (2022).

[47] L. Zhou, Z. Zhuo, L. Kou, A. Du, and S. Tretiak, Nano Lett. **17**, 4466 (2017).

[48] H. Jin, T. Wang, Z.-R. Gong, C. Long, and Y. Dai, Nanoscale **10**, 19310 (2018).

[49] C. Long, Y. Dai, and H. Jin, Phys. Rev. B **104**, 125306 (2021).

[50] J. Jankowska, R. Long, and O. V. Prezhdo, ACS Energy Lett. **2**, 1588 (2017).

[51] H. Guo, W. Chu, Q. Zheng, and J. Zhao, J. Phys. Chem. Lett. **11**, 4662 (2020).

[52] O. V. Prezhdo and P. J. Rossky, Phys. Rev. Lett. **81**, 5294 (1998).

[53] W. Li, J. Liu, F.-Q. Bai, H.-X. Zhang, and O. V. Prezhdo, ACS Energy Lett. **2**, 1270 (2017).

[54] W. Li, J. Tang, D. Casanova, and O. V. Prezhdo, ACS Energy Lett. **3**, 2713 (2018).

[55] R. A. Marcus and N. Sutin, Biochim. Biophys. Acta Rev. Bioenerg. **811**, 265 (1985).

[56] K. Hyeon-Deuk, A. B. Madrid, and O. V. Prezhdo, Dalton Trans. **2009**, 10069 (2009).

[57] L. Li, R. Long, T. Bertolini, and O. V. Prezhdo, Nano Lett. **17**, 7962 (2017).

[58] Q.-q. Li, L. Yan, W. Chu, J. He, H. Luo, T. Frauenheim, S. Tretiak, and L. Zhou, J. Phys. Chem. Lett. **13**, 4955 (2022).